THE JOURNAL OF PHYSICAL CHEMISTRY B
A JOURNAL OF THE AMERICAN CHEMICAL SOCIETY

pubs.acs.org/JPCB

Article

Nanoconfinement between Graphene Walls Suppresses the Near-Wall Diffusion of the Ionic Liquid [BMIM][PF_6]

Cheng Shao, Wee-Liat Ong,* Junichiro Shiomi, and Alan J. H. McGaughey*

Cite This: *J. Phys. Chem. B* 2021, 125, 4527−4535

Read Online

ACCESS | Metrics & More | Article Recommendations | Supporting Information

ABSTRACT: We identify two distinct regimes for the diffusion of the ionic liquid [BMIM][PF_6] confined between parallel graphene walls using molecular dynamics simulations. Within 2 nm of the wall, the cations and anions form a well-defined layered structure. In this region, the in-plane diffusion coefficients are suppressed when compared to their bulk values and increase monotonically with the distance away from the wall. Beyond 2 nm from the wall, the density profile and in-plane diffusion coefficients recover their bulk values. The channel-averaged in-plane diffusion coefficients increase monotonically with wall separation and recover the bulk values at a separation of 15 nm. A simple semianalytical model is proposed that mirrors this trend. The results also highlight the importance of applying a finite-size correction to molecular dynamics-predicted diffusion coefficients of confined liquids, which may otherwise be unusually larger than their bulk values.

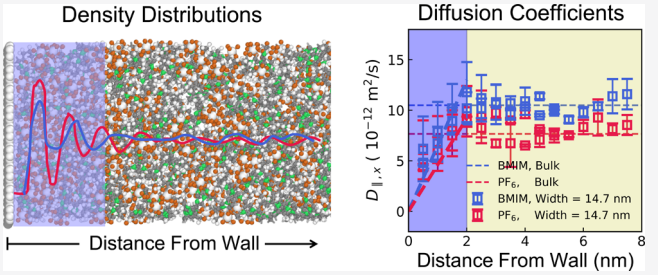

1. INTRODUCTION

Room-temperature ionic liquids (ILs) have attracted attention in energy-related applications due to their unique bulk properties.[1,2] With their high viscosity, low vapor pressure, high thermal and electrochemical stability, and high electrical/proton conductivity, ILs are promising solvents for dye-sensitized solar cells[3−5] and as stabilizing agents/interfacial dopants in hybrid perovskite solar cells.[6−8] ILs are also deployed in energy storage devices such as lithium-ion batteries[9−11] and electrical double-layer capacitors[12−15] due to their nonflammability and wide electrochemical stability window. In such applications, ILs are often confined within micro- and nanostructures,[16,17] which affects their molecular structure, their transport properties, and the device performance.

Experiments and modeling have probed the molecular structure and transport properties of confined liquids,[18,19] with extensive work done on Lennard-Jones (LJ) argon (a toy system)[20,21] and water.[22−26] These studies identified non-continuum characteristics that include confinement-induced abnormal phase transitions,[18,19] spatially varying density profiles near confining surfaces,[22,23] and enhanced mass transport under a pressure gradient.[24−26]

While experimental and modeling studies of bulk ILs have revealed transport physics not found in simple liquids (e.g., bounded cation−anion diffusion[27,28] and molecular caging-induced non-Gaussian transport[29,30]), results for confined ILs are inconsistent.[31−35] Using molecular dynamics (MD) simulations of [DMIM][Cl] confined between two parallel smooth artificial walls, Pinilla et al. predicted a 50 to 100% increase in the average in-plane diffusion coefficient for both the cation and anion compared to the bulk values.[31] The peak enhancement occurred at a wall separation of 2.8 nm. This finding contrasts with the results obtained by Rajput et al. for [EMIM][TFMSI] confined between graphite walls separated by 2.5 and 5.2 nm. From their results, we estimate that the diffusion coefficients were reduced to one third of the bulk values.[32] In a more recent study, Park and McDaniel found that the diffusion coefficients of [BMIM][PF_6] and [BMIM]-[BF_4] confined between graphene walls separated by less than 5 nm are 1 order of magnitude lower than the bulk values and exhibit a maximum when the wall separation is 4 nm.[33] They attributed the nonmonotonic dependence to the coupling of the two electrical double layers, which alters the local ion correlations and dynamics. Contradicting modeling results have also been reported for ILs confined in carbon nanotubes (CNTs). Singh et al. found that the diffusion of [BMIM][PF_6] inside multiwalled CNTs with the inner diameter ranging from 2.0 to 3.7 nm was suppressed as compared to the bulk case.[34] Ghoufi et al. reported an enhancement of 2 orders of magnitude in the diffusion coefficient of [C_4MIM][Tf_2N] confined in a single-walled CNT with a diameter of 2.6 nm.[35]

There are a number of possible origins for differences in the simulated diffusion behavior of confined ILs. First, we note

Received: March 22, 2021
Revised: April 7, 2021
Published: April 22, 2021

https://doi.org/10.1021/acs.jpcb.1c02562
J. Phys. Chem. B 2021, 125, 4527−4535

that the IL density in refs 31, 32, 34 were set to the corresponding bulk value, while ref 35 did not report the density. As a result, the system pressure in these studies, which can influence diffusion, is unknown. Second, the enhanced diffusion reported in some of the MD studies could be caused by the drifting of the center of mass of the confined liquid.[36,37] How to account for this effect is still under debate.[36−39] Third, finite-size corrections to diffusion coefficients are not always applied.[31,33,35] Fourth, as ILs typically have a large viscosity, long simulations (e.g., greater than 100 ns) are required to achieve a converged result.[33,40,41] Otherwise, an overprediction of the diffusion coefficient may occur.

Experimental measurements have also yielded contradicting results.[42,43] From nuclear magnetic resonance spectra line widths in bulk and under confinement inside a monolithic silica matrix, Bideau et al. concluded that the dynamics of [BMIM][TFSI] experienced only a slight slow down at room temperature.[42] Iacob et al., on the other hand, reported an enhancement of 2 orders of magnitude in the diffusion coefficients of [BMIM][BF_4] confined in silica nanopores at a temperature of 180 K.[43] In that study, the diffusion coefficient was estimated using broad-band dielectric spectroscopy measurements.

Motivated by the need for a deeper understanding of the structure and dynamics of confined ILs, we herein describe MD simulations designed to investigate the self-diffusion of an IL confined between two parallel walls. [BMIM][PF_6] was chosen based on its use in energy-related applications[17,44,45] and the availability of experimental and modeling results.[46−48] Two graphene walls separated by 1.8 to 14.7 nm were used to mimic the graphene-based electrodes in some applications.[49,50] Our results show that the effect of a graphene wall penetrates 2 nm into the channel, where it induces IL structuring and impedes mass transport in the near-wall region. Beyond this distance, the local structure and transport recover their bulk nature. At larger wall separations, hydrodynamic self-interaction and finite-size artifacts emerge, leading to a larger-than-bulk in-plane diffusion coefficient that needs to be corrected. We also propose a simple semianalytical model that can predict the channel (i.e., spatially) averaged in-plane diffusion coefficient based on the properties of the ions in the near-wall and bulk-like regions.

The rest of the paper is organized as follows. In Section 2, we describe the interatomic force field, the details of the MD simulations, and the methodologies used to calculate the density distribution, the molecular orientation, and the location-dependent and spatially averaged diffusion coefficients. The bulk IL results are presented in Section 3.1, and the results for the confined IL are presented in Sections 3.2. and 3.3. The findings are summarized in Section 4.

2. METHODS

2.1. Simulation Details. The structures of the $[BMIM]^+$ (1-butyl-3-methylimidazolium, $[C_8H_{15}N_2]^+$, 25 atoms), and $[PF_6]^-$ (7 atoms) ions are shown in Figure 1a. The atomic interactions were modeled using the OPLS-AA force field,[52] which is an all-atom potential that includes bond, angle, dihedral, van der Waals, and electrostatic terms. The charge and interaction parameters refined by Bhargava and Balasubramanian[53] were adopted for $[BMIM]^+$, while the parameters for $[PF_6]^-$ were obtained from Borodin et al.[54] The electrostatic interactions were calculated using an Ewald sum with a real-space cutoff of 1.0 nm and a reciprocal-space force

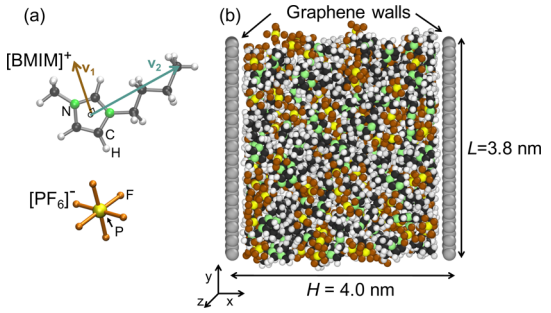

Figure 1. (a) Structures of the $[BMIM]^+$ and $[PF_6]^-$ ions. (b) IL [BMIM][PF_6] confined between two parallel graphene walls separated by a distance H, which here is 4.0 nm. The system is periodic in the y- and z-directions with dimension L = 3.8 nm. The illustration was generated using OVITO.[51]

tolerance of 10^{-6}.[55] For the confined systems, a vacuum gap of 10 nm was added adjacent to the graphene walls to avoid interactions between replicas.[56] The interactions between the ions and the carbon atoms in graphene were described using 12−6 LJ potentials with a cutoff of 1.2 nm. The carbon atoms were charge-neutral and fixed to reduce the computational cost.[25,47] Park and McDaniel found no significant difference when calculating the diffusion coefficients of [BMIM][PF_6] and [BMIM][BF_4] confined between graphene walls that were either insulating (i.e., charge-neutral) or conducting (i.e., representative of an operating electrode).[33] The full form of the force field and its parameters are provided in Section S1 of the Supporting Information.

To build the simulation cell, an example of which is shown in Figure 1b, 60 to 800 [BMIM][PF_6] units were first randomly placed into a rectangular box with one side of length H (x-direction) and the other two sides of length L = 3.8 nm (y- and z-directions) using PACKMOL.[57] Two square graphene sheets with side length L were then placed on the two sides of the box normal to the x-direction. The MD simulations were run using LAMMPS[58] with a time step of 1 fs and periodic boundary conditions in all three directions.

To achieve a zero-pressure configuration, we adjusted the wall separation H in steps of 0.1 Å. The pressure was calculated over 1 ns in the NVT ensemble (i.e., constant number of atoms, volume, and temperature) with a Langevin thermostat at a temperature of 300 K. When the average pressure and its fluctuations fell to 0 ± 100 bar, we deemed the system to be at zero pressure. The resulting zero-pressure wall separations for 10 different systems considered (differentiated by the number of ions) are provided in Table S1.

Previous studies of ILs have suggested that a long simulation time (∼100 ns) is required to achieve statistically converged results.[33,41] To further relax/randomize the structure, we used a "heating-quenching" approach,[41] in which the system was heated to a temperature of 400 K at a rate of 20 K/ns, maintained at 400 K for 10 ns, and then quenched back to 300 K at a rate of 20 K/ns. During this process, the graphene walls were fixed at their zero-pressure positions at 300 K with the temperature controlled by the Langevin thermostat. After the equilibration, we ran simulations in the NVT ensemble for another 200 ns to collect data for the structural and diffusion analyses. For all the location-dependent quantities, averaging was done over symmetric locations across the center of the channel.

https://doi.org/10.1021/acs.jpcb.1c02562
J. Phys. Chem. B 2021, 125, 4527−4535

2.2. Data Collection and Postprocessing. *2.2.1. Distribution of Density, Charge, and Molecular Orientation.* The ionic density distribution in the x-direction was calculated using a bin width of 0.2 nm. For $[BMIM]^+$, density distributions are plotted for the centers of mass of the imidazolium ring and the alkyl tail, while the density distribution for $[PF_6]^-$ is plotted using its center of mass. The charge distribution was calculated based on the charge of each atom using a bin width of 0.1 nm. As shown in Figure 1a, we defined two vectors for analyzing the $[BMIM]^+$ orientation distribution. The first is normal to the imidazole ring ($\mathbf{v}_1$), and the other points from the ring center to the carbon atom at the end of the alkyl tail ($\mathbf{v}_2$). An orientation angle θ is defined as the angle between either $\mathbf{v}_1$ or $\mathbf{v}_2$ and the vector normal to the graphene wall. This angle is used to calculate an orientation order parameter given by the second-order Legendre polynomial $P_2(\cos\theta) = 1.5\cos^2\theta - 0.5$ using a bin width of 0.2 nm.[59,60] As $[PF_6]^-$ is spherically symmetric, we did not quantify its orientation.

2.2.2. Diffusion Coefficient. From the Einstein relation, the diffusion coefficient D in d dimensions can be calculated from the slope of the mean squared displacement (MSD, represented as X^2) of a particle (or a collection of particles) as

$$D = \frac{1}{2d}\lim_{\tau\to\infty}\frac{dX^2(\tau)}{d\tau} \tag{1}$$

where τ is time. The bulk ($d = 3$) diffusion coefficient for each species was calculated from a 5.9 nm cubic simulation box at zero pressure that contained 600 $[BMIM][PF_6]$ units. For each species j, its MSD is averaged over all ions N_j of that same type

$$X_{j,\mathrm{bulk}}{}^2(\tau) = \frac{1}{N_j}\sum_{i=1}^{N_j}\langle |r_{i,x}(\tau) - r_{i,x}(0)|^2 + |r_{i,y}(\tau) - r_{i,y}(0)|^2 + |r_{i,z}(\tau) - r_{i,z}(0)|^2\rangle \tag{2}$$

Here, $r_{i,\alpha}(\tau)$ is the position of ion i in the α-direction (i.e., x, y, or z) at time τ. The angular brackets denote an ensemble average obtained using 150 different samples. Each sample consists of a 50 ns window started every 1 ns for the first 150 ns of the 200 ns simulation.

To calculate the spatially averaged in-plane diffusion coefficients ($d = 2$) for a wall separation H, $D_{j,\|,H}$, the confined IL model described in Section 2.1 was used to obtain the in-plane MSD from

$$X_{j,\|,H}{}^2(\tau) = \frac{1}{N_j}\sum_{i=1}^{N_j}\langle |r_{i,y}(\tau) - r_{i,y}(0)|^2 + |r_{i,z}(\tau) - r_{i,z}(0)|^2\rangle \tag{3}$$

The spatially averaged cross-plane diffusion coefficient ($d = 1$), $D_{j,\perp,H}$, was calculated from the cross-plane MSD as

$$X_{j,\perp,H}{}^2(\tau) = \frac{1}{N_j}\sum_{i=1}^{N_j}\langle |r_{i,x}(\tau) - r_{i,x}(0)|^2\rangle \tag{4}$$

Because the momentum of the confined IL is not conserved due to interactions with the wall, we subtracted the center-of-mass displacement of the ions of species j when applying eqs 3 and 4.

Under parallel confinement, the in-plane diffusion coefficient can vary based on the distance from the wall.[61] A location-dependent in-plane diffusion coefficient, $D_{j,\|,x}$, can be obtained by tracking the ions in layers parallel to the confining wall.[62,63] To do so, we partitioned the channel along the x-direction into virtual layers, each with a width of 1 nm. This layer width is a compromise between the spatial resolution and the resulting uncertainty. We then counted the number of ions $N_{j,x}(\tau)$ that originated and stayed in the layer centered at position x over a time period τ. The survival probability $P_{j,x}(\tau)$ of the ions in that layer is then defined as[62]

$$P_{j,x}(\tau) = \frac{N_{j,x}(\tau)}{N_{j,x}(0)} \tag{5}$$

where $N_{j,x}(0)$ is the number of ions of type j in that layer at the start time. As we will show in Section 3.3, the survival probability can be fit using the sum of two exponential decays, resulting in two time constants that are associated with decay processes with distinct physical origins.

From the survival probability, the subset of ions $\mathfrak{R}_{j,x}(\tau)$ remaining in a layer centered at position x after time τ is equal to $P_{j,x}(\tau)N_{j,x}(0)$. The in-plane MSD required to calculate the diffusion coefficient can then be calculated from

$$X_{j,\|,x}{}^2(\tau) = \frac{1}{N_x(0)P_x(\tau)}\sum_{i\in\mathfrak{R}_{j,x}(\tau)}\langle |r_{i,y}(\tau) - r_{i,y}(0)|^2 + |r_{i,z}(\tau) - r_{i,z}(0)|^2\rangle \tag{6}$$

In evaluating eq 6, we subtracted the center-of-mass motion of the species j ions within the layer.

To evaluate the above MSD equations, we used the real particle displacements without accounting for the periodic boundary conditions. The diffusion coefficient in eq 1 was fit from the linear portion of the MSD.[64] The error bars in the subsequent results are from the uncertainty in the postprocessing fitting process. The spatially averaged diffusion coefficients were extracted for times from 10 to 50 ns. For the location-dependent diffusion coefficients, as the number of ions that remain within a certain layer decays with time, we extracted the diffusion coefficients for times from 0.5 to 2 ns.[65] We estimate that this choice leads to a 10% overprediction based on convergence studies. See Figure S6 of the Supporting Information for more details and the convergence study with respect to the relaxation time and the time used for MSD fitting.

2.2.3. Diffusion Coefficient Size Effects. Due to the long-range nature of the hydrodynamic interaction, diffusion coefficients calculated using a finite simulation box with periodic boundary conditions will generally suffer from a finite-size effect.[66−68] This size effect arises from the truncation of the long-wavelength modes and can lead to an underestimation of the diffusion coefficient for a fully periodic cubic box. A typical way to compensate for this finite-size effect is to start from the Navier−Stokes equation of an incompressible fluid to obtain the Oseen tensor $\mathbf{T}$ of a finite periodic system and compare it with that of an infinite nonperiodic system.[66−68] The difference between these two Oseen tensors is related to the difference in the diffusion coefficient tensor (the correction term $\Delta\mathbf{D}$) through $\Delta\mathbf{D} = k_B T\Delta\mathbf{T}$, where k_B is the Boltzmann constant.[66] For a cubic simulation box with periodic boundary conditions, Yeh and Hummer derived that[66]

$$D_{\mathrm{bulk}} = D_{\mathrm{PBC}}(L) + \frac{\xi k_B T}{6\pi\eta L} \tag{7}$$

https://doi.org/10.1021/acs.jpcb.1c02562
J. Phys. Chem. B 2021, 125, 4527−4535

where D_{bulk} is the corrected bulk diffusion coefficient, $D_{PBC}(L)$ is the bulk diffusion coefficient from a periodic cubic box of length L, η is the viscosity (see calculation details in Section S3), and ξ is a constant obtained from the Ewald summation over the periodic images and is equal to 2.837 for a cubic simulation box.[66]

The finite-size effect for the diffusion coefficient under confinement is more nuanced. Here, the simulation box is periodic in the in-plane directions but constrained by confining walls in the cross-plane direction such that it is typically noncubic. Beyond the abovementioned hydrodynamic effect, an additional size effect arises due to the thermal fluctuations of the liquid's center of mass. This effect comes from the nonconservation of momentum in the system due to the forces exerted by the confining wall.[36,37] These two effects typically result in an overprediction of diffusion coefficients.[36−38] Analogous to the periodic cubic case, the finite-size effect under parallel confinement can be obtained by comparing the Oseen tensor of a parallelly confined system with a lateral length of L to that of a bulk system.[38] Simonnin et al. derived a correction for the spatially averaged in-plane diffusion coefficient for an elongated parallelly confined system to be[38]

$$D_{\parallel,\infty}(H) = D_{\parallel,L}(H) + \frac{k_B T}{\eta}\left[\frac{3\ln(1+\sqrt{2})}{4\pi L} - \frac{7}{60}\frac{H}{L^2}\right] \quad (8)$$

Here, $D_{\parallel,\infty}(H)$ is the corrected in-plane diffusion coefficient for a wall separation H and $D_{\parallel,L}(H)$ is the in-plane diffusion coefficient of the confined simulation domain with a lateral length L and wall separation H. The first term inside the square brackets represents the self-interaction term and the second term corresponds to the summation of hydrodynamic interactions between the periodic images in the Fourier space. Because we have subtracted the center-of-mass effect when calculating the MSD,[39] eq 8 does not include the additional term $H/(24L^2)$ inside the square brackets as originally proposed by Simonnin et al.[38] We did not apply eq 8 to the location-dependent diffusion coefficient, which was calculated using a 1 nm thick fluid layer, as the continuum assumption behind the derivation of eq 8 may not be valid.[38]

3. RESULTS AND DISCUSSION

3.1. Bulk Properties. The bulk properties of [BMIM][PF_6] at a temperature of 300 K obtained from our simulations and previous studies are summarized in Table 1. Our calculated density and shear viscosity (see details in Section S3) are 1390 kg/m^3 (2.92 ions/nm^3 for both $[BMIM]^+$ and $[PF_6]^-$) and 0.14 ± 0.01 Pa·s, which compare well with previous results.[47,53,69] Our bulk diffusion coefficients calculated from a 5.9 nm cubic box at zero pressure and corrected using eq 7 are 10.5 ± 0.5 × 10^{-12} m^2/s for $[BMIM]^+$ and 7.7 ± 0.5 × 10^{-12} m^2/s for $[PF_6]^-$. The correction term has a value of +0.8 × 10^{-12} m^2/s. This correction was not included in the previous simulation studies, causing their diffusion coefficients to be generally smaller than ours. Assuming that these previous studies used a cubic simulation box with a side length of 3 to 5 nm and a shear viscosity similar to ours (these data are not available in those studies), a correction of 0.8−1.6 × 10^{-12} m^2/s would be added to their diffusion coefficients. Factors that may account for the remaining differences include the difference in the force field used, the pressure of the simulation box, and insufficient simulation time to obtain converged results. Our predicted diffusion coefficients for $[BMIM]^+$ and $[PF_6]^-$ are around 30% larger than the experimental measurements,[46] as also found in other simulation studies, which may be a result of the force field used. The reasonable agreement between our bulk predictions and those of previous studies gave us confidence to proceed with studying confinement effects on [BMIM][PF_6].

Table 1. Density, Diffusion Coefficients, and Shear Viscosity of Bulk [BMIM][PF_6] from Simulations and Experiments at a Temperature of 300 K

density (kg/m^3)	diffu. coeff. (×10^{-12} m^2/s) $[BMIM]^+$	diffu. coeff. (×10^{-12} m^2/s) $[PF_6]^-$	shear viscosity (Pa·s)	notes
1390	10.5 ± 0.5	7.7 ± 0.5	0.14 ± 0.01	MD (this work)
1368	12.9	9.0	0.14 ± 0.01	MD[69]
	9.7 ± 4.1	8.8 ± 4.2		MD[70]
1380	9.2	6.7		MD[47]
1389	6.7	4.7		MD[53]
	6.9	5.2		experiment[71]
1369	8.0	5.9	0.23	experiment[46]
1362			0.21	experiment[72]

3.2. Distribution of Density, Charge, and Molecular Orientation. The ionic density distributions of $[BMIM]^+$ and $[PF_6]^-$ confined in a channel with a wall separation of 9.9 nm are plotted in Figure 2a, with the bulk value plotted as a dashed horizontal line. Both $[BMIM]^+$ and $[PF_6]^-$ show a layered structure with an oscillating density profile that decays to the bulk value away from the wall. Similar layered structures are found for other wall separations in this study (Figure S2) and are commonly observed for confined liquids.[20,73−76] As the graphene walls are charge-neutral, we attribute this near-wall layered structure to the large electrostatic interactions between the IL molecules in the presence of the weak van der Waals wall−liquid interactions. The first dense layer modifies the potential energy landscape for the surrounding ions, leading to the formation of the second maximum. This effect propagates but weakens with distance away from the wall. For both $[BMIM]^+$ and $[PF_6]^-$, the density profiles become bulk-like at a distance of 2 nm from the wall. We thus divided the confined channel into two regions: the skin region, which has a thickness of 2 nm (purple shading), and the bulk-like region (yellow shading). As we will show in Section 3.3.1, the transport properties also differ in these two regions. The $[PF_6]^-$ density profile exhibits larger oscillations than that of $[BMIM]^+$, which may be due to the combined effects of a smaller van der Waals radius and a stronger interaction strength with graphene.

Similarities in the locations but differences in the magnitudes for the first density maxima and minima of $[BMIM]^+$ and $[PF_6]^-$ indicate a nonuniform charge distribution, as shown in Figure 2b. The sharp peak at 0.4 nm is mainly contributed by $[PF_6]^-$. We note that the charge distribution forms near a charge-neutral surface and is thus a consequence of the layering effect. This behavior differs from the electrical double layer that typically exists near a charged surface.[77,78] The charge distribution creates a potential barrier, which may impede ion exchange between the first density maximum and minimum. While the density fluctuations persist up to 2 nm from the graphene wall, the charge fluctuations return to their bulk values by a distance of 1 nm. Beyond this distance, the

https://doi.org/10.1021/acs.jpcb.1c02562
J. Phys. Chem. B 2021, 125, 4527−4535

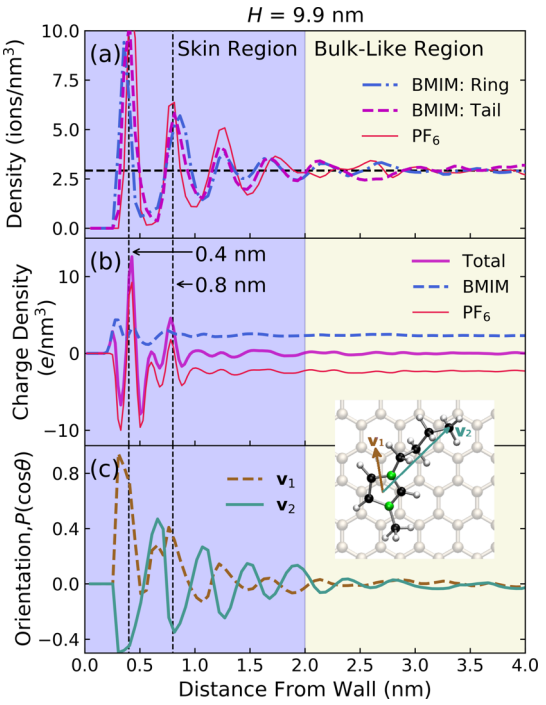

Figure 2. Distributions of (a) density, (b) charge, and (c) molecular orientation of $[BMIM]^+$ and $[PF_6]^-$ under confinement between two graphene walls with a separation H of 9.9 nm. The two vertical dashed lines at 0.4 and 0.8 nm mark an in-phase correlation between the density, charge, and orientation distributions. For $[BMIM]^+$, the density profiles are plotted using the centers of mass of the imidazolium ring (Ring) and the alkyl tail (Tail). The inset of (c) shows the preferred orientation of $[BMIM]^+$ near the wall, where the imidazolium ring and the alkyl tail are parallel to the wall. The purple shading indicates the skin region, and the yellow shading indicates the bulk-like region.

density extrema are slightly offset [Figure 2a] and the ions screen one another.

To further elucidate the near-wall IL structure, the orientation order parameter $P(\cos\theta)$ for $[BMIM]^+$ is plotted in Figure 2c. A value of 1 indicates that the chosen vector [$\mathbf{v}_1$ or $\mathbf{v}_2$ in the inset of Figure 2c] is perpendicular to the graphene wall while a value of −0.5 indicates that this vector is parallel to the graphene wall. Note that $\mathbf{v}_1$ and $\mathbf{v}_2$ are perpendicular to each other. As shown in Figure 2c, the $[BMIM]^+$ ions have a preferred orientation at a distance of 0.4 nm from the wall that coincides with the first density maximum. This result indicates that the $[BMIM]^+$ ions tend to orient with their imidazolium ring and the alkyl tail parallel to the graphene wall, as illustrated in the inset of Figure 2c. In this orientation, $[BMIM]^+$ achieves a maximum binding energy of 0.6 eV with the graphene wall (Figure S3). Similar preferred orientations have been observed for other imidazolium ring-containing cations in vibrational spectroscopy experiments.[79] Preferred orientations are also observed at distances of 0.8 and 1.2 nm from the graphene wall, which also coincide with the density maxima.

3.3. Diffusion Coefficients. *3.3.1. Location-Dependent.* The structural properties plotted in Figure 2a-c suggest location-dependent dynamics in confined $[BMIM][PF_6]$. The dense layer and potential barrier in the skin region should hinder the ionic dynamics through dimensional restriction,[21,75] which lengthens an ion's residence time in a layer. To test this hypothesis, we used eq 5 to calculate the survival probability of the $[BMIM]^+$ and $[PF_6]^-$ ions as a function of the distance from the wall. The number of ions that remains in a layer decreases with increasing time. The corresponding decay rate reflects the likelihood of an ion leaving at a certain time. We find that the survival probability for each ion type can be described using the sum of two exponential decays in the form:

$$f(t) = a\exp^{-t/\tau_f} + b\exp^{-t/\tau_s} \quad (9)$$

where a, b, the fast decay time constant τ_f, and the slow decay time constant τ_s are fitting parameters.[80,81] The fitting results for a wall separation of 14.7 nm are plotted in Figure S4. This functional form was also used by Feng et al. to extract the residence time of free and bound ions in bulk $[BMIM][PF_6]$.[28]

The fast decay time constant represents the timescale required for an ion to escape from the cage formed by its neighbors.[47] It is 0.15 ± 0.05 ns in all the layers for all wall separations (Figure S5). The slow decay time constant represents the timescale for an ion to escape a layer and will be directly affected by the local density. It is plotted for both ions for wall separations of 9.9 and 14.7 nm in Figure 3a,b. At a distance of 0.5 nm from the wall, the slow decay time constant is ∼15 ns, which is 2 orders of magnitude larger than the fast decay time constant. Consistent with the decay of the density maxima and minima values to the bulk values shown in Figure 2a, a similar behavior is observed for the slow decay time constant. For both $[BMIM]^+$ and $[PF_6]^-$, the slow decay time constant decreases monotonically with increasing distance from the wall and reaches the bulk value at around 2 nm. The slow decay time constants for $[BMIM]^+$ and $[PF_6]^-$, which are on the order of nanoseconds, are large when compared to the picosecond values found in liquid LJ argon near a solid wall.[82]

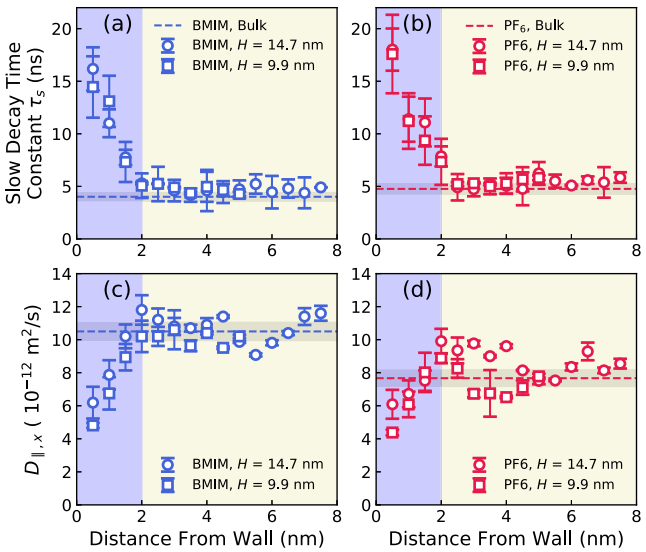

Figure 3. Slow decay time constants of (a) $[BMIM]^+$ and (b) $[PF_6]^-$ and layer-dependent in-plane diffusion coefficients of (c) $[BMIM]^+$ and (d) $[PF_6]^-$ in channels with wall separations of 9.9 and 14.7 nm. The horizontal dashed lines are the corresponding bulk values. The gray-shaded region represents the uncertainty in the bulk values. The purple shading indicates the skin region, and the yellow shading indicates the bulk-like region. We did not apply the finite size correction [eq 8] for the location-dependent diffusion coefficient in (c,d), which may explain the slightly above-bulk prediction away from the wall.

https://doi.org/10.1021/acs.jpcb.1c02562
J. Phys. Chem. B 2021, 125, 4527−4535

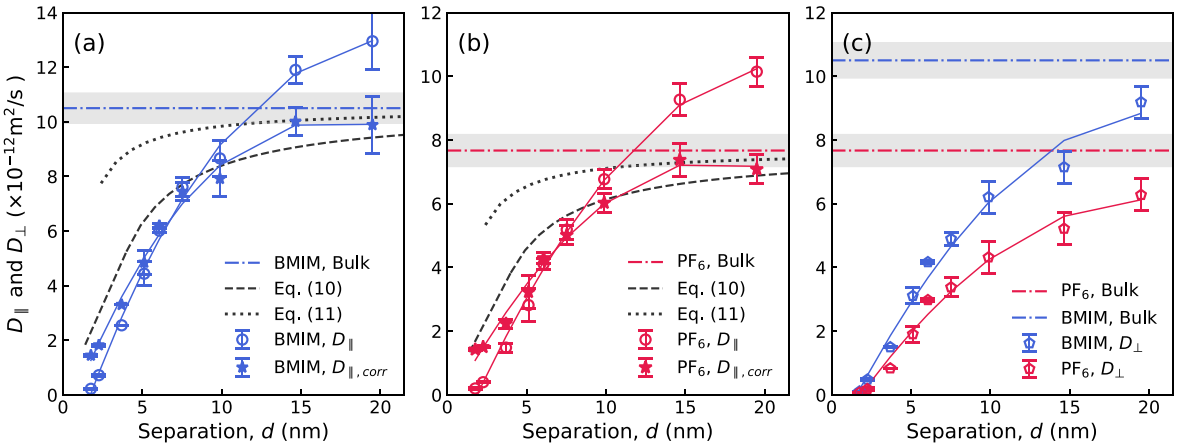

Figure 4. Spatially averaged (a,b) in-plane ($D_\parallel$) and (c) cross-plane ($D_\perp$) diffusion coefficients of $[BMIM]^+$ and $[PF_6]^-$ as a function of the wall separation. The horizontal lines are the bulk diffusion coefficients after the finite size correction, and the gray area represents the uncertainty in the bulk diffusion coefficients. The open circles are uncorrected diffusion coefficients, while the filled stars are corrected in-plane diffusion coefficients using eq 8. Solid lines accompanying the simulation data points are drawn to guide the eye.

The longer time constant results from the strong electrostatic interactions and the complex molecular geometry of [BMIM]-[PF_6], which sterically hinders the ionic motions.[28]

The slow decay time constant is closely related to the diffusion properties. As shown in Figure 3c,d, the location-dependent in-plane diffusion coefficient for both $[BMIM]^+$ and $[PF_6]^-$ increases with increasing distance from the wall until the bulk value is reached at a distance of 2 nm. Comparing Figure 3c,d to 3a,b, it is clear that larger slow decay time constants correspond to lower diffusion coefficients. The transition at 2 nm seen in Figure 3a−d is consistent with those in the density, charge, and orientation distributions shown in Figure 2a−c. This consistency further validates our decision to divide the channel effect into the skin region, where confinement effects are present, and the bulk-like region. The location-dependent slow decay time constant, which can be easily obtained from the survival probability [eq 5], can serve as a criterion to determine the skin thickness.

3.3.2. Spatially Averaged. Experimentally, a spatially averaged in-plane diffusion coefficient, instead of the location-dependent values, is more readily accessible. We calculated the spatially averaged in-plane values using eq 3, and the results are plotted in Figure 4a,b as a function of the wall separation as open circles. The data increase monotonically toward the bulk value and then exceed it, without reaching a constant value. By applying the correction given by eq 8, we obtain the diffusion coefficients plotted as solid stars, which reach a constant value that falls within the uncertainties of the bulk values for wall separations greater than 15 nm. In studying [BMIM][PF_6] confined between graphene walls separated by less than 5 nm, Park and McDaniel observed a local maximum in the diffusion coefficient at a wall separation of 4 nm, which they attributed to the coupling of the two electrical double layers.[33] We do not observe such a local maximum, which may be due to our coarser resolution of the wall separation.

With the insight gained from the location-dependent diffusion coefficients, we explore the possibility of estimating the spatially averaged in-plane diffusion coefficient in a confined system by using a weighted average of the average diffusion coefficients in the skin and bulk regions. Based on Figure 3c,d, we assume that the location-dependent diffusion coefficient increases linearly from zero to the bulk value within the skin thickness. Beyond the skin thickness, we take the diffusion coefficient to be equal to the bulk value. Based on this dual-regime (DR) description, we propose to calculate the spatially averaged in-plane diffusion coefficient from

$$D_{\parallel,\mathrm{DR}}(H) = \begin{cases} \dfrac{H}{4d} D_{\mathrm{bulk}}, & \text{for } H < 2d \\ \dfrac{H-d}{H} D_{\mathrm{bulk}}, & \text{for } H \geq 2d \end{cases} \tag{10}$$

where d is the skin thickness. The resulting predictions are plotted in Figure 4a,b. Compared to the corrected in-plane diffusion coefficients from the MD simulations, the predictions from eq 10 overpredict the diffusion coefficient for wall separations less than 10 nm but underpredict above that. The overall trend from MD is well-captured by eq 10 with the largest deviation of ~20% for a wall separation of 5 nm. The larger deviations at the small wall separations may be because the location-dependent diffusion coefficients used in eq 10 are calculated from a subset of the ions in a thin layer.

Wang and Hadjiconstantinou used a similar analytical approach to evaluate the in-plane diffusion coefficient of LJ argon under confinement and found good agreement with their MD simulation results.[75] In their model, they assumed that all fluid particles outside the first-layer region (defined as the region beyond the first peak in the density profile; see Figure 2a) exhibit the bulk diffusion coefficient, leading to

$$D_{\parallel,\mathrm{FL}}(H) = D_{\mathrm{bulk}}\left(1 - \frac{2d_{\mathrm{FL}}}{H}\right) + D_{\mathrm{FL}}\frac{2d_{\mathrm{FL}}}{H} \tag{11}$$

where d_{FL} is the thickness of the first-layer (FL) region and D_{FL} is the diffusion coefficient in the FL. We denote eq 11 as the FL model. Based on Figure 2a, d_{FL} is taken as 0.6 nm for both ions. D_{FL} is estimated to be 5×10^{-12} and 3×10^{-12} m^2/s for $[BMIM]^+$ and $[PF_6]^-$ from Figure 3c,d, The predictions from eq 11 are plotted as dotted lines in Figure 4a,b. Compared to our DR model [eq 10], the FL model significantly overpredicts the diffusion coefficient for small wall separations but agrees better with the MD results when the wall separation is larger than 15 nm. The larger deviation of the MD results with the

https://doi.org/10.1021/acs.jpcb.1c02562
J. Phys. Chem. B 2021, 125, 4527−4535

FL model at smaller wall separation indicates that the confinement effect penetrates beyond the first density layer, which is better captured by our DR model. Still, the difference between the two analytical models and the MD results suggests that while a simple model can qualitatively capture the overall trend of the spatially averaged in-plane diffusion coefficient under confinement, finer fluid dynamics details must be included to achieve better quantitative agreement.

The spatially averaged cross-plane diffusion coefficients are plotted in Figure 4c. The cross-plane values are lower than the corresponding values in the in-plane direction, except for the extreme confinement scenario of 1.8 nm. Even for the largest wall separation considered here of 19.5 nm, the spatially averaged cross-plane diffusion coefficients are around 15% lower than the bulk values. Based on the observed trend, we estimate that a wall separation of at least ∼30 nm will be required for the cross-plane diffusion coefficients to recover their bulk value.

4. CONCLUSIONS

We investigated the structure and dynamics of the IL [BMIM][PF_6] confined between two parallel graphene walls using MD simulations. We identified a critical length scale of 2 nm (i.e., the skin thickness) within which nonbulk characteristics are present. Ions in the skin thickness form a layered structure [Figure 2a] with preferred orientations [Figure 2c], creating an electrostatic potential barrier [Figure 2b], and exhibit larger slow decay time constants and smaller diffusion coefficients [Figure 3a−d]. For ions beyond the skin thickness, their structural and dynamical properties are bulk-like. This dual diffusion regime description suggests that a simple weighted average equation may be appropriate for estimating the spatially averaged in-plane diffusion coefficient [Figure 4a,b]. The raw MD data overpredict the in-plane diffusion coefficient, a bias that arises from a combination of the hydrodynamic interaction of periodic images and movement of the IL's center-of-mass. The corrections given by eq 7[66] and 8[38] are required to obtain physically meaningful results. Also of critical importance are careful selection of the system size to establish a zero pressure and sufficiently long simulations to ensure relaxed structures and converged statistics.

Our results provide clear evidence that the location-dependent in-plane diffusion coefficients are smaller than the bulk value within 2 nm of the graphene wall and approach the bulk values beyond this distance. After applying the corrections given by eqs 7 and 8, no enhanced diffusion coefficients when compared to bulk values are detected anywhere in the channel. We note that in previous MD studies on confined ILs showing enhanced diffusion,[31,35] such a correction is not applied, which may partly contribute to their conclusions. Our results suggest that when using ILs in an energy-conversion nanodevice, one needs to consider the confinement-induced suppression in diffusion coefficient when the confining feature size is less than O (10 nm). Our proposed diffusion model can qualitatively and quantitatively capture such nanoscale diffusion behavior of ILs. As most energy-conversion devices employing ILs will have ILs confined in nanopores or nanostructures near the electrode surfaces, our nanoscale diffusion results will facilitate their design, fabrication, and solution processing.

■ ASSOCIATED CONTENT

Supporting Information

The Supporting Information is available free of charge at https://pubs.acs.org/doi/10.1021/acs.jpcb.1c02562.

Force field used in simulations; wall separation and pressure; shear viscosity calculations; density distribution at different wall separations; energy minimization of $[BMIM]^+$ on a graphene wall; survival probability and the fast decay time; and convergence studies for the diffusion coefficient calculations (PDF)

Detailed force field parameters for the MD simulation in LAMMPS (TXT)

Atomic structure of one [BMIM][PF_6] (XYZ)

■ AUTHOR INFORMATION

Corresponding Authors

Wee-Liat Ong − *ZJU-UIUC Institute, College of Energy Engineering, Zhejiang University, Haining, Zhejiang 314400, People's Republic of China; State Key Laboratory of Clean Energy Utilization, Zhejiang University, Hangzhou, Zhejiang 310027, China*; Email: weeong@intl.zju.edu.cn

Alan J. H. McGaughey − *Department of Mechanical Engineering, Carnegie Mellon University, Pittsburgh, Pennsylvania 15213, United States*; orcid.org/0000-0002-0118-6893; Email: mcgaughey@cmu.edu

Authors

Cheng Shao − *Department of Mechanical Engineering, Carnegie Mellon University, Pittsburgh, Pennsylvania 15213, United States; University of Michigan−Shanghai Jiao Tong University Joint Institute, Shanghai Jiao Tong University, Shanghai 200240, China; Department of Mechanical Engineering, The University of Tokyo, Tokyo 113-8656, Japan*; orcid.org/0000-0002-4382-2608

Junichiro Shiomi − *Department of Mechanical Engineering, The University of Tokyo, Tokyo 113-8656, Japan*; orcid.org/0000-0002-3552-4555

Complete contact information is available at: https://pubs.acs.org/10.1021/acs.jpcb.1c02562

Notes

The authors declare no competing financial interest.

■ ACKNOWLEDGMENTS

C.S. acknowledges the China Scholarships Council for support for the portion of the work done at Carnegie Mellon University. W.-L. Ong was as one of the principal supervisors supported by the National Natural Science Foundation of China (grant: 51876186), Natural Science Foundation of Zhejiang Province (Key grant: LZ19E060002), the Fundamental Research Funds for the Central Universities (K20200145), and ZJU-UIUC Institute. We thank Gerald J. Wang at Carnegie Mellon University for helpful discussion. The calculations in this work were partially performed using supercomputer facilities of the Institute for Solid State Physics, University of Tokyo, and MASAMUNE-IMR at the Center for Computational Materials Science, Institute for Materials Research, Tohoku University (Project nos. 2012SC0507 and 2012SC0510).

REFERENCES

(1) Galiński, M.; Lewandowski, A.; Stpniak, I. Ionic Liquids as Electrolytes. *Electrochim. Acta* **2006**, *51*, 5567−5580.
(2) Zhang, Q.; Shreeve, J. M. Energetic Ionic Liquids as Explosives and Propellant Fuels: A New Journey of Ionic Liquid Chemistry. *Chem. Rev.* **2014**, *114*, 10527−10574.
(3) Wang, P.; Zakeeruddin, S. M.; Moser, J.-E.; Grätzel, M. A New Ionic Liquid Electrolyte Enhances the Conversion Efficiency of Dye-Sensitized Solar Cells. *J. Phys. Chem. B* **2003**, *107*, 13280−13285.
(4) Wang, P.; Zakeeruddin, S. M.; Comte, P.; Exnar, I.; Grätzel, M. Gelation of Ionic Liquid-Based Electrolytes With Silica Nanoparticles for Quasi-Solid-State Dye-Sensitized Solar Cells. *J. Am. Chem. Soc.* **2003**, *125*, 1166−1167.
(5) Ito, S.; Zakeeruddin, S. M.; Humphry-Baker, R.; Liska, P.; Charvet, R.; Comte, P.; Nazeeruddin, M. K.; Péchy, P.; Takata, M.; Miura, H.; et al. High-Efficiency Organic-Dye-Sensitized Solar Cells Controlled by Nanocrystalline-TiO_2 Electrode Thickness. *Adv. Mater.* **2006**, *18*, 1202−1205.
(6) Bai, S.; Da, P.; Li, C.; Wang, Z.; Yuan, Z.; Fu, F.; Kawecki, M.; Liu, X.; Sakai, N.; Wang, J. T.-W.; Huettner, S.; Buecheler, S.; Fahlman, M.; Gao, F.; Snaith, H. J. Planar Perovskite Solar Cells With Long-Term Stability Using Ionic Liquid Additives. *Nature* **2019**, *571*, 245−250.
(7) Ghosh, S.; Singh, T. Role of Ionic Liquids in Organic-Inorganic Metal Halide Perovskite Solar Cells Efficiency and Stability. *Nano Energy* **2019**, *63*, 103828.
(8) Salado, M.; Jodlowski, A. D.; Roldan-Carmona, C.; de Miguel, G.; Kazim, S.; Nazeeruddin, M. K.; Ahmad, S. Surface Passivation of Perovskite Layers Using Heterocyclic Halides: Improved Photovoltaic Properties and Intrinsic Stability. *Nano Energy* **2018**, *50*, 220−228.
(9) Zhao, L.; Hu, Y.-S.; Li, H.; Wang, Z.; Chen, L. Porous $Li_4Ti_5O_{12}$ Coated With N-Doped Carbon From Ionic Liquids for Li-Ion Batteries. *Adv. Mater.* **2011**, *23*, 1385−1388.
(10) Huie, M. M.; DiLeo, R. A.; Marschilok, A. C.; Takeuchi, K. J.; Takeuchi, E. S. Ionic Liquid Hybrid Electrolytes for Lithium-Ion Batteries: A Key Role of the Separator-Electrolyte Interface in Battery Electrochemistry. *ACS Appl. Mater. Interfaces* **2015**, *7*, 11724−11731.
(11) Usui, H.; Domi, Y.; Fujiwara, K.; Shimizu, M.; Yamamoto, T.; Nohira, T.; Hagiwara, R.; Sakaguchi, H. Charge−Discharge Properties of a Sn_4P_3 Negative Electrode in Ionic Liquid Electrolyte for Na-Ion Batteries. *ACS Energy Lett.* **2017**, *2*, 1139−1143.
(12) Mousavi, M. P. S.; Wilson, B. E.; Kashefolgheta, S.; Anderson, E. L.; He, S.; Bühlmann, P.; Stein, A. Ionic Liquids as Electrolytes for Electrochemical Double-Layer Capacitors: Structures That Optimize Specific Energy. *ACS Appl. Mater. Interfaces* **2016**, *8*, 3396−3406.
(13) Vijayakumar, M.; Schwenzer, B.; Shutthanandan, V.; Hu, J.; Liu, J.; Aksay, I. A. Elucidating Graphene−Ionic Liquid Interfacial Region: A Combined Experimental and Computational Study. *Nano Energy* **2014**, *3*, 152−158.
(14) Merlet, C.; Rotenberg, B.; Madden, P. A.; Taberna, P.-L.; Simon, P.; Gogotsi, Y.; Salanne, M. On the Molecular Origin of Supercapacitance in Nanoporous Carbon Electrodes. *Nat. Mater.* **2012**, *11*, 306−310.
(15) Largeot, C.; Portet, C.; Chmiola, J.; Taberna, P.-L.; Gogotsi, Y.; Simon, P. Relation Between the Ion Size and Pore Size for an Electric Double-Layer Capacitor. *J. Am. Chem. Soc.* **2008**, *130*, 2730−2731.
(16) Zhang, S.; Zhang, J.; Zhang, Y.; Deng, Y. Nanoconfined Ionic Liquids. *Chem. Rev.* **2016**, *117*, 6755−6833.
(17) Perkin, S. Ionic Liquids in Confined Geometries. *Phys. Chem. Chem. Phys.* **2012**, *14*, 5052.
(18) Koga, K.; Tanaka, H.; Zeng, X. C. First-Order Transition in Confined Water Between High-Density Liquid and Low-Density Amorphous Phases. *Nature* **2000**, *408*, 564−567.
(19) Koga, K.; Gao, G. T.; Tanaka, H.; Zeng, X. C. Formation of Ordered Ice Nanotubes Inside Carbon Nanotubes. *Nature* **2001**, *412*, 802−805.
(20) Gao, J.; Luedtke, W. D.; Landman, U. Layering Transitions and Dynamics of Confined Liquid Films. *Phys. Rev. Lett.* **1997**, *79*, 705−708.
(21) Wang, G. J.; Hadjiconstantinou, N. G. Molecular Mechanics and Structure of the Fluid-Solid Interface in Simple Fluids. *Phys. Rev. Fluids* **2017**, *2*, 094201.
(22) McGaughey, A. J. H.; Mattia, D. Materials Enabling Nanofluidic Flow Enhancement. *MRS Bull.* **2017**, *42*, 273−277.
(23) Thomas, J. A.; McGaughey, A. J. H. Density, Distribution, and Orientation of Water Molecules Inside and Outside Carbon Nanotubes. *J. Chem. Phys.* **2008**, *128*, 084715.
(24) Holt, J. K. Fast Mass Transport Through Sub-2-Nanometer Carbon Nanotubes. *Science* **2006**, *312*, 1034−1037.
(25) Thomas, J. A.; McGaughey, A. J. H. Reassessing Fast Water Transport Through Carbon Nanotubes. *Nano Lett.* **2008**, *8*, 2788−2793.
(26) Falk, K.; Sedlmeier, F.; Joly, L.; Netz, R. R.; Bocquet, L. Molecular Origin of Fast Water Transport in Carbon Nanotube Membranes: Superlubricity Versus Curvature Dependent Friction. *Nano Lett.* **2010**, *10*, 4067−4073.
(27) Lee, A. A.; Vella, D.; Perkin, S.; Goriely, A. Are Room-Temperature Ionic Liquids Dilute Electrolytes? *J. Phys. Chem. Lett.* **2014**, *6*, 159−163.
(28) Feng, G.; Chen, M.; Bi, S.; Goodwin, Z. A.; Postnikov, E. B.; Brilliantov, N.; Urbakh, M.; Kornyshev, A. A. Free and Bound States of Ions in Ionic Liquids, Conductivity, and Underscreening Paradox. *Phys. Rev. X* **2019**, *9*, 021024.
(29) Casalegno, M.; Raos, G.; Appetecchi, G. B.; Passerini, S.; Castiglione, F.; Mele, A. From Nanoscale to Microscale: Crossover in the Diffusion Dynamics Within Two Pyrrolidinium-Based Ionic Liquids. *J. Phys. Chem. Lett.* **2017**, *8*, 5196−5202.
(30) Skaug, M. J.; Mabry, J.; Schwartz, D. K. Intermittent Molecular Hopping at the Solid-Liquid Interface. *Phys. Rev. Lett.* **2013**, *110*, 256101.
(31) Pinilla, C.; Del Pópolo, M. G.; Lynden-Bell, R. M.; Kohanoff, J. Structure and Dynamics of a Confined Ionic Liquid. Topics of Relevance to Dye-Sensitized Solar Cells. *J. Phys. Chem. B* **2005**, *109*, 17922−17927.
(32) Rajput, N. N.; Monk, J.; Singh, R.; Hung, F. R. On the Influence of Pore Size and Pore Loading on Structural and Dynamical Heterogeneities of an Ionic Liquid Confined in a Slit Nanopore. *J. Phys. Chem. C* **2012**, *116*, 5169−5181.
(33) Park, S.; McDaniel, J. G. Interference of Electrical Double Layers: Confinement Effects on Structure, Dynamics, and Screening of Ionic Liquids. *J. Chem. Phys.* **2020**, *152*, 074709.
(34) Singh, R.; Monk, J.; Hung, F. R. A Computational Study of the Behavior of the Ionic Liquid $[BMIM^+][PF6^-]$ Confined Inside Multiwalled Carbon Nanotubes. *J. Phys. Chem. C* **2010**, *114*, 15478−15485.
(35) Ghoufi, A.; Szymczyk, A.; Malfreyt, P. Ultrafast Diffusion of Ionic Liquids Confined in Carbon Nanotubes. *Sci. Rep.* **2016**, *6*, 28518.
(36) Detcheverry, F.; Bocquet, L. Thermal Fluctuations in Nanofluidic Transport. *Phys. Rev. Lett.* **2012**, *109*, 024501.
(37) Detcheverry, F.; Bocquet, L. Thermal Fluctuations of Hydrodynamic Flows in Nanochannels. *Phys. Rev. E: Stat., Nonlinear, Soft Matter Phys.* **2013**, *88*, 012106.
(38) Simonnin, P.; Noetinger, B.; Nieto-Draghi, C.; Marry, V.; Rotenberg, B. Diffusion Under Confinement: Hydrodynamic Finite-Size Effects in Simulation. *J. Chem. Theory Comput.* **2017**, *13*, 2881−2889.
(39) Zaragoza, A.; Gonzalez, M. A.; Joly, L.; López-Montero, I.; Canales, M. A.; Benavides, A. L.; Valeriani, C. Molecular Dynamics Study of Nanoconfined TIP4P/2005 Water: How Confinement and Temperature Affect Diffusion and Viscosity. *Phys. Chem. Chem. Phys.* **2019**, *21*, 13653−13667.
(40) Maginn, E. J. Atomistic Simulation of the Thermodynamic and Transport Properties of Ionic Liquids. *Acc. Chem. Res.* **2007**, *40*, 1200−1207.
(41) Wu, F.; Karunaratne, W. V.; Margulis, C. J. Ionic Liquid Mixture at the Vacuum Interface and the Peaks and Antipeaks

https://doi.org/10.1021/acs.jpcb.1c02562
J. Phys. Chem. B 2021, 125, 4527−4535

Analysis of X-Ray Reflectivity. *J. Phys. Chem. C* **2019**, *123*, 4914−4925.
(42) Bideau, J. L.; Gaveau, P.; Bellayer, S.; Néouze, M.-A.; Vioux, A. Effect of Confinement on Ionic Liquids Dynamics in Monolithic Silica Ionogels: 1h NMR Study. *Phys. Chem. Chem. Phys.* **2007**, *9*, 5419.
(43) Iacob, C.; Sangoro, J. R.; Kipnusu, W. K.; Valiullin, R.; Kärger, J.; Kremer, F. Enhanced Charge Transport in Nano-Confined Ionic Liquids. *Soft Matter* **2012**, *8*, 289−293.
(44) Chaurasia, S. K.; Saroj, A. L.; Shalu; Singh, V. K.; Tripathi, A. K.; Gupta, A. K.; Verma, Y. L.; Singh, R. K. Studies on Structural, Thermal and AC Conductivity Scaling of PEO-$LiPF_6$ Polymer Electrolyte With Added Ionic Liquid [$BMIMPF_6$]. *AIP Adv.* **2015**, *5*, 077178.
(45) Armand, M.; Endres, F.; MacFarlane, D. R.; Ohno, H.; Scrosati, B. Ionic-liquid materials for the electrochemical challenges of the future. *Materials for Sustainable Energy*; Macmillan Publishers Ltd: UK, 2010; pp 129−137. DOI: 10.1142/9789814317665_0020
(46) Tokuda, H.; Hayamizu, K.; Ishii, K.; Susan, M. A. B. H.; Watanabe, M. Physicochemical Properties and Structures of Room Temperature Ionic Liquids. 1. Variation of Anionic Species. *J. Phys. Chem. B* **2004**, *108*, 16593−16600.
(47) Singh, R.; Monk, J.; Hung, F. R. Heterogeneity in the Dynamics of the Ionic Liquid [$BMIM^+$][$PF6^-$] Confined in a Slit Nanopore. *J. Phys. Chem. C* **2011**, *115*, 16544−16554.
(48) Dou, Q.; Sha, M.; Fu, H.; Wu, G. Melting Transition of Ionic Liquid [$BMIM^+$][$PF6^-$] Crystal Confined in Nanopores: A Molecular Dynamics Simulation. *J. Phys. Chem. C* **2011**, *115*, 18946−18951.
(49) Liu, C.; Yu, Z.; Neff, D.; Zhamu, A.; Jang, B. Z. Graphene-Based Supercapacitor With an Ultrahigh Energy Density. *Nano Lett.* **2010**, *10*, 4863−4868.
(50) Simon, P.; Gogotsi, Y. *Nanoscience and Technology*; Macmillan Publishers Ltd: UK, 2009; pp 320−329.
(51) Stukowski, A. Visualization and analysis of atomistic simulation data with OVITO-the Open Visualization Tool. *Modell. Simul. Mater. Sci. Eng.* **2009**, *18*, 015012.
(52) Canongia Lopes, J. N.; Pádua, A. A. H. Molecular Force Field for Ionic Liquids III: Imidazolium, Pyridinium, and Phosphonium Cations; Chloride, Bromide, and Dicyanamide Anions. *J. Phys. Chem. B* **2006**, *110*, 19586−19592.
(53) Bhargava, B. L.; Balasubramanian, S. Refined Potential Model for Atomistic Simulations of Ionic Liquid [$BMIM^+$][$PF6^-$]. *J. Chem. Phys.* **2007**, *127*, 114510.
(54) Borodin, O.; Smith, G. D.; Jaffe, R. L. Ab initio quantum chemistry and molecular dynamics simulations studies of LiPF6/poly(ethylene oxide) interactions. *J. Comput. Chem.* **2001**, *22*, 641−654.
(55) Essmann, U.; Perera, L.; Berkowitz, M. L.; Darden, T.; Lee, H.; Pedersen, L. G. A Smooth Particle Mesh Ewald Method. *J. Chem. Phys.* **1995**, *103*, 8577−8593.
(56) Yeh, I.-C.; Wallqvist, A. On the Proper Calculation of Electrostatic Interactions in Solid-Supported Bilayer Systems. *J. Chem. Phys.* **2011**, *134*, 055109.
(57) Martínez, L.; Andrade, R.; Birgin, E. G.; Martínez, J. M. PACKMOL: A Package for Building Initial Configurations for Molecular Dynamics Simulations. *J. Comput. Chem.* **2009**, *30*, 2157−2164.
(58) Plimpton, S. Fast Parallel Algorithms for Short-Range Molecular Dynamics. *J. Comput. Phys.* **1995**, *117*, 1−19.
(59) Fedorov, M. V.; Lynden-Bell, R. M. Probing the neutral graphene-ionic liquid interface: insights from molecular dynamics simulations. *Phys. Chem. Chem. Phys.* **2012**, *14*, 2552.
(60) Ori, G.; Massobrio, C.; Pradel, A.; Ribes, M.; Coasne, B. Structure and Dynamics of Ionic Liquids Confined in Amorphous Porous Chalcogenides. *Langmuir* **2015**, *31*, 6742−6751.
(61) Mittal, J.; Truskett, T. M.; Errington, J. R.; Hummer, G. Layering and Position-Dependent Diffusive Dynamics of Confined Fluids. *Phys. Rev. Lett.* **2008**, *100*, 145901.
(62) Liu, P.; Harder, E.; Berne, B. J. On the Calculation of Diffusion Coefficients in Confined Fluids and Interfaces With an Application to the Liquid−Vapor Interface of Water. *J. Phys. Chem. B* **2004**, *108*, 6595−6602.
(63) Wick, C. D.; Dang, L. X. Diffusion at the Liquid−Vapor Interface of an Aqueous Ionic Solution Utilizing a Dual Simulation Technique. *J. Phys. Chem. B* **2005**, *109*, 15574−15579.
(64) Berne, B. J.; Harp, G. On the Calculation of Time Correlation Functions. *Adv. Chem. Phys.* **1970**, *17*, 63−227.
(65) von Hansen, Y.; Gekle, S.; Netz, R. R. Anomalous Anisotropic Diffusion Dynamics of Hydration Water at Lipid Membranes. *Phys. Rev. Lett.* **2013**, *111*, 118103.
(66) Yeh, I.-C.; Hummer, G. System-Size Dependence of Diffusion Coefficients and Viscosities From Molecular Dynamics Simulations With Periodic Boundary Conditions. *J. Phys. Chem. B* **2004**, *108*, 15873−15879.
(67) Dünweg, B.; Kremer, K. Molecular Dynamics Simulation of a Polymer Chain in Solution. *J. Chem. Phys.* **1993**, *99*, 6983−6997.
(68) Kikugawa, G.; Nakano, T.; Ohara, T. Hydrodynamic Consideration of the Finite Size Effect on the Self-Diffusion Coefficient in a Periodic Rectangular Parallelepiped System. *J. Chem. Phys.* **2015**, *143*, 024507.
(69) Zhao, W.; Leroy, F.; Balasubramanian, S.; Müller-Plathe, F. Shear Viscosity of the Ionic Liquid 1-n-Butyl 3-Methylimidazolium Hexafluorophosphate [bmim][PF6] Computed by Reverse Non-equilibrium Molecular Dynamics. *J. Phys. Chem. B* **2008**, *112*, 8129−8133.
(70) Morrow, T. I.; Maginn, E. J. Molecular Dynamics Study of the Ionic Liquid 1-N-Butyl-3-Methylimidazolium Hexafluorophosphate. *J. Phys. Chem. B* **2002**, *106*, 12807−12813.
(71) Kanakubo, M.; Harris, K. R.; Tsuchihashi, N.; Ibuki, K.; Ueno, M. Effect of Pressure on Transport Properties of the Ionic Liquid 1-Butyl-3-Methylimidazolium Hexafluorophosphate. *J. Phys. Chem. B* **2007**, *111*, 2062−2069.
(72) Jacquemin, J.; Husson, P.; Padua, A. A. H.; Majer, V. Density and Viscosity of Several Pure and Water-Saturated Ionic Liquids. *Green Chem.* **2006**, *8*, 172−180.
(73) Thompson, P. A.; Robbins, M. O. Origin of Stick-Slip Motion in Boundary Lubrication. *Science* **1990**, *250*, 792−794.
(74) Bhushan, B.; Israelachvili, J. N.; Landman, U. Nanotribology: Friction, Wear and Lubrication at the Atomic Scale. *Nature* **1995**, *374*, 607−616.
(75) Wang, G. J.; Hadjiconstantinou, N. G. Layered Fluid Structure and Anomalous Diffusion Under Nanoconfinement. *Langmuir* **2018**, *34*, 6976−6982.
(76) Gao, J.; Luedtke, W. D.; Landman, U. Origins of Solvation Forces in Confined Films. *J. Phys. Chem. B* **1997**, *101*, 4013−4023.
(77) Fedorov, M. V.; Kornyshev, A. A. Towards Understanding the Structure and Capacitance of Electrical Double Layer in Ionic Liquids. *Electrochim. Acta* **2008**, *53*, 6835−6840.
(78) Shim, Y.; Kim, H. J.; Jung, Y. Graphene-Based Supercapacitors in the Parallel-Plate Electrode Configuration: Ionic Liquidsversus Organic Electrolytes. *Faraday Discuss.* **2012**, *154*, 249−263.
(79) Fitchett, B. D.; Conboy, J. C. Structure of the Room-Temperature Ionic Liquid/SiO2Interface Studied by Sum-Frequency Vibrational Spectroscopy. *J. Phys. Chem. B* **2004**, *108*, 20255−20262.
(80) Kob, W.; Donati, C.; Plimpton, S. J.; Poole, P. H.; Glotzer, S. C. Dynamical Heterogeneities in a Supercooled Lennard-Jones Liquid. *Phys. Rev. Lett.* **1997**, *79*, 2827−2830.
(81) Metzler, R.; Klafter, J. The Random Walk's Guide to Anomalous Diffusion: A Fractional Dynamics Approach. *Phys. Rep.* **2000**, *339*, 1−77.
(82) Thomas, J. A.; McGaughey, A. J. H. Effect of Surface Wettability on Liquid Density, Structure, and Diffusion Near a Solid Surface. *J. Chem. Phys.* **2007**, *126*, 034707.

https://doi.org/10.1021/acs.jpcb.1c02562
J. Phys. Chem. B 2021, 125, 4527−4535